ACS OMEGA

http://pubs.acs.org/journal/acsodf

Article

Crab Shell-Derived SnS_2/C and FeS_2/C Carbon Composites as Anodes for High-Performance Sodium-Ion Batteries

Yun Chen,* Yue Zhao, Hongbin Liu,* and Tingli Ma*

Cite This: *ACS Omega* 2023, 8, 9145−9153

Read Online

ACCESS | Metrics & More | Article Recommendations | Supporting Information

ABSTRACT: The demand for energy storage devices has increased significantly, and the sustainable development of lithium-ion batteries is limited by scarce lithium resources. Therefore, alternative sodium-ion batteries which are rich in resource may become more competitive in the future market. In this work, we synthesized low-cost SnS_2/C and FeS_2/C anode materials of sodium-ion batteries which used waste crab shells as biomass carbon precursor. The SnS_2 nanosheet and FeS_2 nanosphere structures are deposited on the crab shell-derived carbon through simple hydrothermal reaction. Due to the coexistence of transition metal dichalcogenides (TMDs) and crab-derived biomass carbon, the anode material has excellent cycle stability and rate performance. SnS_2/C and FeS_2/C deliver capacities of 535.4 and 479 mA h g^{-1} at the current density of 0.1 A g^{-1}, respectively. This study explored an effective and economical strategy to use biomass and TMDs to construct high-performance sodium-ion batteries.

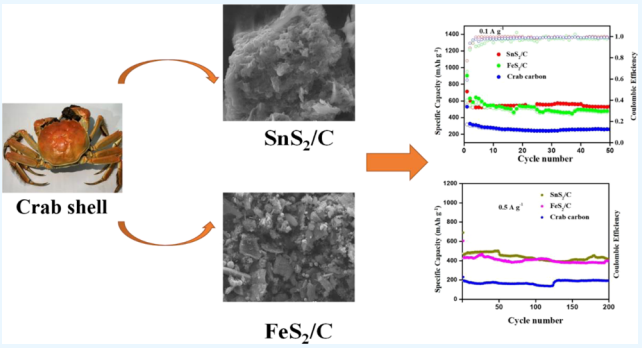

INTRODUCTION

Owing to its high energy density and long cycle life, lithium-ion batteries have been widely used in the field of portable energy storage devices.[1−5] However, their sustainable development is limited by scarce lithium resources.[6] Therefore, alternative devices may become more competitive in the future market, especially for large energy storage systems such as electric vehicles and fixed grid storage.[7−13] Compared with lithium, sodium is rich in resource and low in cost, and its redox potential is relatively close to that of lithium, so sodium-ion battery has high expectations on the application of large-scale energy storage systems.[14−18] Currently, graphene is the most widely used anode material for lithium batteries. However, due to the large radius of sodium ions (0.95 Å Na^+ is larger than 0.60 Å Li^+) that makes insertion difficult, graphite almost has no sodium storage activity. At present, widely studied sodium-ion battery anode materials include hard carbon, metals, metal oxides/sulfides, alloys, organic compounds, and so forth.[19−22]

Among TMDs, Sn-based transition-metal sulfides have been extensively studied because of their high theoretical capacity (1136 mA h g^{-1}). The high capacity of Sn-based transition-metal sulfide is attributed to the combined effect of the conversion reaction and the alloying reaction. However, the poor conductivity of the Sn-based sulfide anode materials limits their electrochemical performance. The Fe-based transition-metal sulfide has a high theoretical capacity of 894 mA h g^{-1} and has been extensively studied due to its low cost and non-toxic characteristics.[9,23−26] Although SnS_2 and FeS_2 have high theoretical capacities, they are far from expected in actual applications. During alloying reactions, there are significant volume expansion, crushing, and mechanical deformation, which result in poor cycle stability and capacity.[27] The active materials are easy to coarsen, which hugely limits the progress of the reverse reaction and interferes with the energy density of the sodium-ion batteries (SIBs) adversely.[28−34]

Generally, there are three common ways to improve sodium-ion storage for sodium-ion batteries: (1) composite TMDs with carbon materials. The excellent conductivity of carbon materials can not only promote the transmission of Na^+ but also provide a buffer layer for volume expansion during the conversion process and consequently improve cycle stability and rate performance. (2) Regulating the morphology of transition-metal sulfides. A good structure can shorten the diffusion distance of sodium ions, providing enough space for volume expansion. (3) Constructing bimetallic sulfide. Compared with monometallic sulfide, bimetallic sulfide contains more active sites, and the constructed heterojunction

Received: October 5, 2022
Accepted: November 30, 2022
Published: February 28, 2023

https://doi.org/10.1021/acsomega.2c06429
ACS Omega 2023, 8, 9145−9153

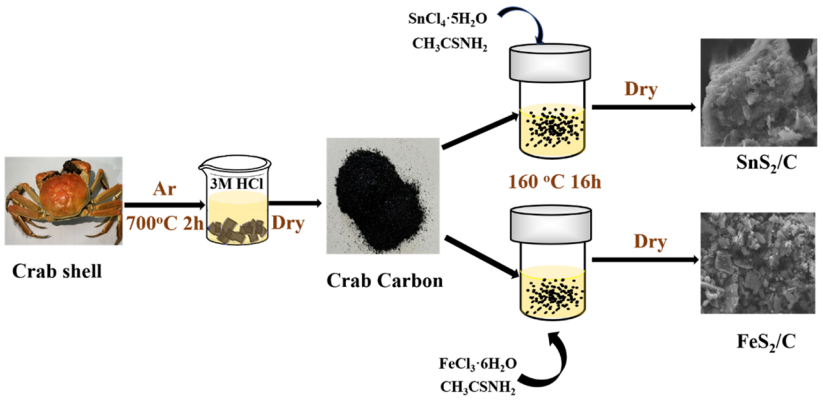

Figure 1. Schematic illustration of the fabrication process of the crab carbon and SnS_2/C and FeS_2/C composites.

can further improve the electrical conductivity and enhance the electrochemical performance. (4) Selection of suitable electrolytes. A suitable electrolyte which affects the formation of the solid electrolyte interface (SEI) is an important factor in determining the battery performance.[35]

Recently, biomass-derived hard carbon materials have attracted widespread attention as electrode materials for SIBs because of the superior performance, eco-friendliness, abundance, and renewability. However, the low theoretical capacity limits its application. Therefore, a strategy that combines TMDs and biomass-based hard carbon can not only improve cycle stability but also have a higher capacity and a lower cost, thus providing a better solution for industrialization.[33,36−38]

Herein, we synthesized SnS_2/C and FeS_2/C composites which used waste crab shell as hard carbon biomass precursor. SnS_2 nanosheet and FeS_2 nanosphere structures are deposited on the crab shell-derived carbon through a simple hydrothermal reaction. Due to the coexistence of metal sulfides and crab carbon with a high surface area, the composite material has excellent cycle performance and rate capability and has long-term stability. When used as the anode of sodium-ion batteries, SnS_2/C and FeS_2/C deliver the capacities of 416.5 and 393.8 mA h g^{-1} at the current density of 0.5 mA g^{-1}, respectively, after 200 cycles. This study provides an economical strategy to use biomass and TMDs to construct high-performance sodium-ion batteries.

EXPERIMENT SECTION

Synthesis of Crab Carbon. Crab carbon was prepared by one-step carbonization of crab shell (Figure 1). The pretreated crab shell was carbonized at 700 °C for 2 h under the atmosphere of Ar gas. After purification in 3 M HCl solution, washing by deionized water, and drying at 120 °C overnight in a vacuum oven, the crab carbon was obtained.

Synthesis of SnS_2/C and FeS_2/C Composite Materials. The SnS_2/C and FeS_2/C composites were prepared by a facile hydrothermal method (Figure 1). First, 30 mL of deionized water and 20 mL of ethanol were mixed with stirring for 2 h. 0.7 g of $SnCl_4·5H_2O$ was added dropwise to the solution to form Sn^{4+} solution. Then 0.45 g of CH_3CSNH_2, 2 mL of acetic acid (HAc), and 0.8 g of the as-prepared crab carbon were added to the Sn^{4+} solution. The above solution was transferred to a Teflon-lined autoclave and kept at 160 °C for 16 h. Finally, the product composite was washed twice with water and ethanol and then freeze-dried for 24 h. The synthesized method of FeS_2/C is the same as that of SnS_2/C using 0.54 g of $FeCl_3·5H_2O$ as a reagent.

RESULTS AND DISCUSSION

We first used X-ray diffraction (XRD) patterns to analyze the composition and purity of the synthesized crab carbon and

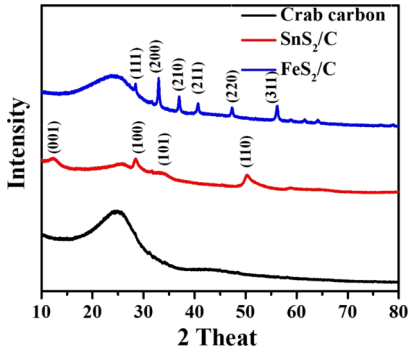

Figure 2. XRD pattern of crab carbon and SnS_2/C and FeS_2/C composites.

SnS_2/C and FeS_2/C composites (Figure 2). The strong and broad diffraction peaks in the crab carbon sample indicate that it has amorphous graphitic phase. SnS_2/C has broad diffraction peaks and the diffraction peaks of (001), (100), (101), and (110) lattice planes, which are in good agreement with SnS_2 (JCPDS no. 23-0677). The pattern of FeS_2/C has the broad diffraction peaks which belong to amorphous carbon, and the diffraction peaks of (111), (200), (210), (211), (220), and (311) are attributed to FeS_2 (JCPDS no. 23-0677). This shows that our synthesized product does not contain other impurities, and the target samples are obtained.

The scanning electron microscopy (SEM) images show that the morphology of crab carbon is a porous hierarchical layered structure (Figure 3a,b). After 700 °C carbonization, the chitin protein nanofibers in crab shell transformed into carbon skeleton. Crab carbon exhibits a typical 3D interconnected honeycomb hierarchical structure and contains a lot of pores, which greatly increases the specific surface area.[39−43] Compared with the flat porous structure of crab carbon, the SnS_2/C sample has a superimposed multilayer porous structure (Figure 3c,d), which is beneficial for the sodiation and desodiation of sodium ions. FeS_2/C is constituted by FeS_2 nanospheres and porous crab carbon (Figure 3e). Moreover,

https://doi.org/10.1021/acsomega.2c06429
ACS Omega 2023, 8, 9145−9153

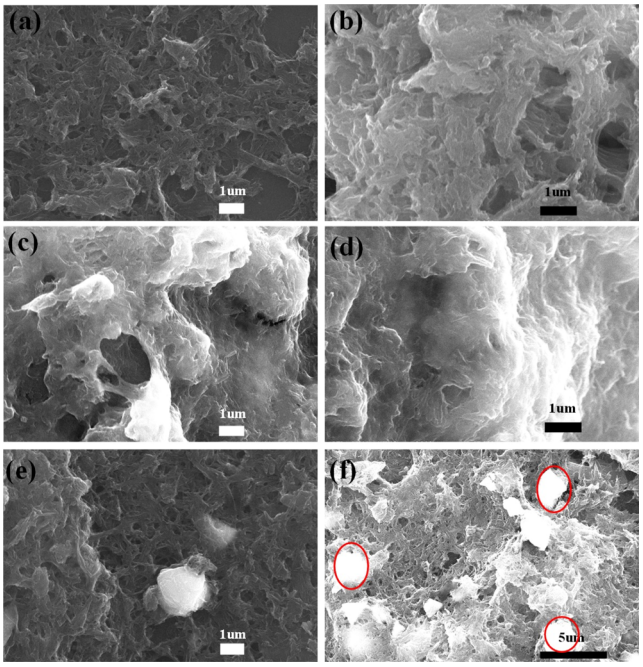

Figure 3. Morphology and structural characterization of SEM images of (a,b) crab carbon, (c,d) SnS_2/C, and (e,f) FeS_2/C.

FeS_2 nanospheres are uniformly distributed on the surface of crab carbon (Figure 3f).

Transmission electron microscopy (TEM) was used to analyze the future details of the SnS_2/C and FeS_2/C composites. It shows that SnS_2/C composite has many fibers with a pore structure, which is crab carbon precursor, and the SnS_2 nanosheets which are evenly distributed on the surface of crab carbon (Figure 4a,b). It shows that on a smaller scale, the SnS_2 layered structure is composed of nanosheets. This nanofiber pore and nanosheet hybrid structure not only shorten the sodium-ion transmission distance but also reduce electrical resistance and provide more buffer layers for volume expansion. Energy-dispersive X-ray spectroscopy (EDX) element mapping displays that the elements of S, Sn, and C are evenly distributed on the surface of SnS_2/C composite (Figure 4c–f).

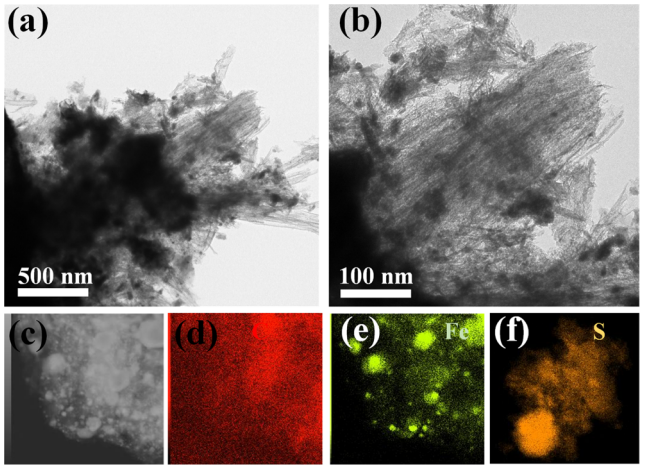

Figure 5. Morphology and structural characterization: (a,b) TEM images and (c–f) elemental mapping images of FeS_2/C composite.

It shows that FeS_2/C composite is constituted of nanofibers (crab carbon) and nanospheres (FeS_2) (Figure 5a,b). EDX element mapping displays that the elements of S, Fe, and C are distributed on the surface of SnS_2/C composite (Figure 5c–f). This proves that the structure and morphology of crab do not change when it compounds with Sn_2S and Fe_2S.

From the Raman spectrums (Figure 6a), two peaks appear at 1340 and 1575 cm^{-1}, which are related to disordered carbon (D band) and graphitic carbon (G band), respectively. The ratio of I_G/I_D represents the degree of graphitization of the sample. The analysis shows that the I_G/I_D of the three samples are very close. It also indicates that crab carbon does not change much after compounding sulfides. Brunauer–Emmett–Teller (BET) method displays that crab carbon (272 $m^2\ g^{-1}$) has a larger surface area than SnS_2/C (186 $m^2\ g^{-1}$) and FeS_2 (102 $m^2\ g^{-1}$) (Figure 6b). The large specific surface area of crab carbon can provide more ion transport channels, which is

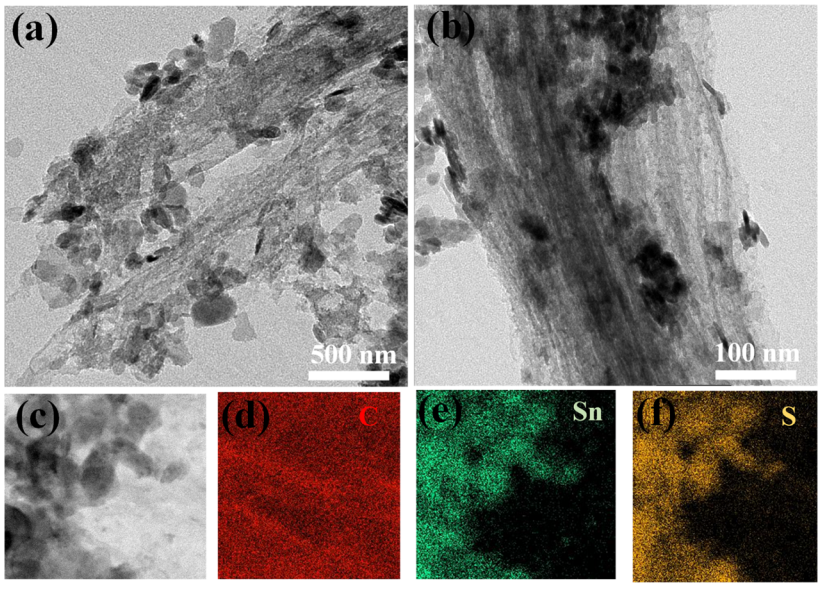

Figure 4. Morphology and structural characterization: (a,b) TEM images and (c–f) elemental mapping images of SnS_2/C composite.

https://doi.org/10.1021/acsomega.2c06429
ACS Omega 2023, 8, 9145–9153

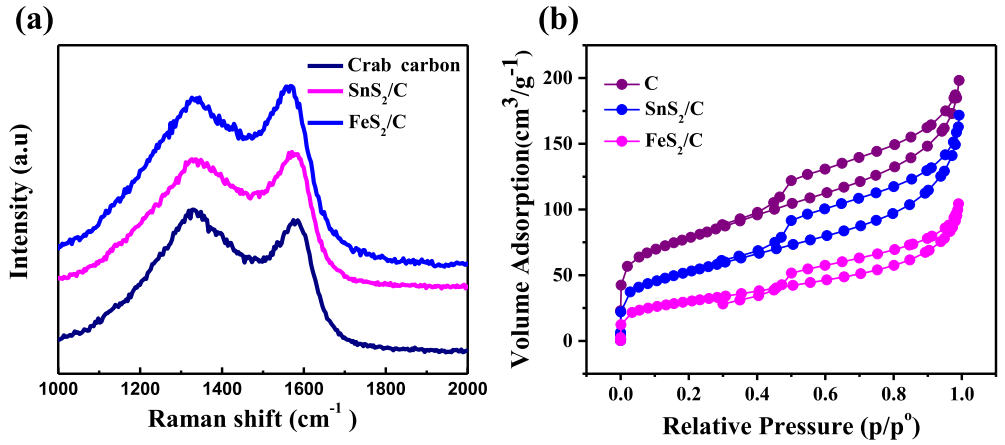

Figure 6. (a) Raman spectra and (b) nitrogen adsorption−desorption isotherms of crab carbon, SnS_2/C, and FeS_2/C samples.

conducive to the fast transport of sodium ions. Compared with the nanosphere structure of FeS_2, the nanosheet structure of SnS_2 provides a larger specific surface area.

X-ray photoelectron spectroscopy can further analyze the element composition and surface electronic state of the sample. As shown in Figure 7a, it clearly indicates that FeS_2/C contains the elements of S, O, C, and Fe. The presence of O can be attributed to the oxidation of the sample in the air. For Fe 2p spectrum (Figure 7c), the peaks at 719.9 eV and 707 eV can be attributed to the presence of Fe^{2+} and 711.1 eV corresponds to Fe^{3+}. For the S 2p spectrum (Figure 7e), it can be divided into two peaks at 162.8 eV ($2P_{1/2}$) and 161.7 eV ($2P_{3/2}$), which correspond to S^{2-} (FeS_2). For SnS_2/C sample (Figure 7b), it contains the elements of C, Sn, and S. The Sn 3d spectrum (Figure 7d) contains the peaks at 486.6 and 495.1 eV which can be attributed to Sn $3d_{5/2}$, and Sn $3d_{3/2}$, respectively. For the S 2p spectrum (Figure 7f), it can also be divided into two peaks at 163.6 eV ($2P_{1/2}$) and 162.4 eV ($2P_{3/2}$) which correspond to S^{2-} (SnS_2).

Figure 8a,b shows the charge−discharge curves of the SnS_2/C and FeS_2/C composites during the initial three cycles at a current density of 0.1 A g^{-1}. For SnS_2/C anode material, the specific capacities of the first cycle of discharge and charge are 713.4 and 550.1 mA h g^{-1}, respectively, corresponding to 77% of initial Coulombic efficiency. The specific capacities of the first cycle of FeS_2/C composite discharge and charge are 903.2 mA h g^{-1} and 603.9 mA h g^{-1}, respectively, corresponding to 66.8% of initial Coulombic efficiency. To further demonstrate the superiority of the SnS_2/C and FeS_2/C anode materials, we have tested the electrochemical properties of different samples and compare them in Figure 8c,d. The crab carbon, SnS_2/C, and FeS_2/C deliver capacities of 262.5, 535.4, and 479 mA h g^{-1} at the current density of 0.1 A g^{-1} after 50 cycles, respectively. After compounding with sulfide, the composite still exhibits good stability and the specific capacity has been significantly improved. When the current density increased from 0.1 to 0.5 A g^{-1}, crab carbon, SnS_2/C, and FeS_2/C deliver the capacities of 192.3, 416.5, and 393.8 mA h g^{-1}, respectively, after 200 cycles (Figure 8d). The capacity retention rate of SnS_2/C is 60%, and that of FeS_2/C is 64%. This means that the synthesized composite material has good stability under a large current density and has the potential for fast charging applications. Figure 8e,f shows the rate performance recover ability of SnS_2/C and FeS_2/C electrode materials. For SnS_2/C anode, the specific capacities are 572.8, 465.2, 329.3, 243.4, and 167.6 mA h g^{-1} at the currently densities of 0.1, 0.2, 0.5, 1, and 2 A g^{-1}, respectively. When the current density returns to 0.1 A g^{-1}, the specific capacity returns to 552 mA h g^{-1}, indicating that the composite material has excellent rate performance. The result shows that the specific capacity of the battery under the rate performance is not as good as the direct current test. For FeS_2/C electrode material, the specific capacities are 567.5, 460.2, 339.5, 220.5, and 220.5 mA h g^{-1} at the current densities of 0.1, 0.2, 0.5, 1, and 2 A g^{-1}, respectively. When the current density returns to 0.1A g^{-1}, the specific capacity returns to 482.2 mA h g^{-1}. It proves that the FeS_2/C composite anode also has good recover capacity.

The cyclic voltammetry (CV) test was used to analyze the reactions of electrode materials during cycling, which was scanned at 0.1 mV s^{-1} between 0.01 and 3.0 V, as shown in Figure 9. For SnS_2/C, the cathodic scan of the first cycle, a strong peak around 1.0 V is due to the conversion reaction [$SnS_2 + Na^+ \rightarrow Na_xSnS_2$ ($x < 2$)] and the formation of SEI.[44] A weak peak around 0.2 V is attributed to the conversion reaction ($Na_xSnS_2 \rightarrow Sn^0 + Na_2S$).[45] For the anodic scan of the other cycles, the peak around 1.6 V is due to the form of Na_xSnS_2 and the SEI layers. The peak around 2.3 V can be ascribed to the reaction of Sn^0/Na_2S and irreversible SEI layer (Figure 9a). For FeS_2, the resulting redox reaction is similar to that of SnS_2, the reduction peak is at 1.1 V, and oxidation peaks are around 1.4 and 2.2 V (Figure 9b).

We used electrochemical impedance spectroscopy (EIS) to analyze the conductivity of the electrode materials in the sodium-ion batteries. Figure 10 shows that the spectrum can be divided into three parts. The semicircle in the high-frequency region represents the diffusion resistance R_{sei} when Na^+ passes through the SEI membrane. The semicircle in the middle-frequency area represents the charge-transfer resistance R_{ct}. The oblique line in the low-frequency area is the solid-state diffusion process. After the first cycle, the charge transmission resistance of crab carbon is larger than that of FeS_2/C and SnS_2/C. It means that the SnS_2/C and FeS_2/C composite structures are more conducive to Na^+ transmission (Figure 10a). After the 200th, the Na^+ transmission resistance of crab carbon is smaller than that of FeS_2/C and SnS_2/C (Figure 10b). This proves that the crab carbon that contains abundant nanofiber channels is conducive to maintaining a stable structure, keeping good contact with the current collector during cycles. The FeS_2/C and SnS_2/C are accompanied by volume expansion during cycles, causing extrusion and

https://doi.org/10.1021/acsomega.2c06429
ACS Omega 2023, 8, 9145−9153

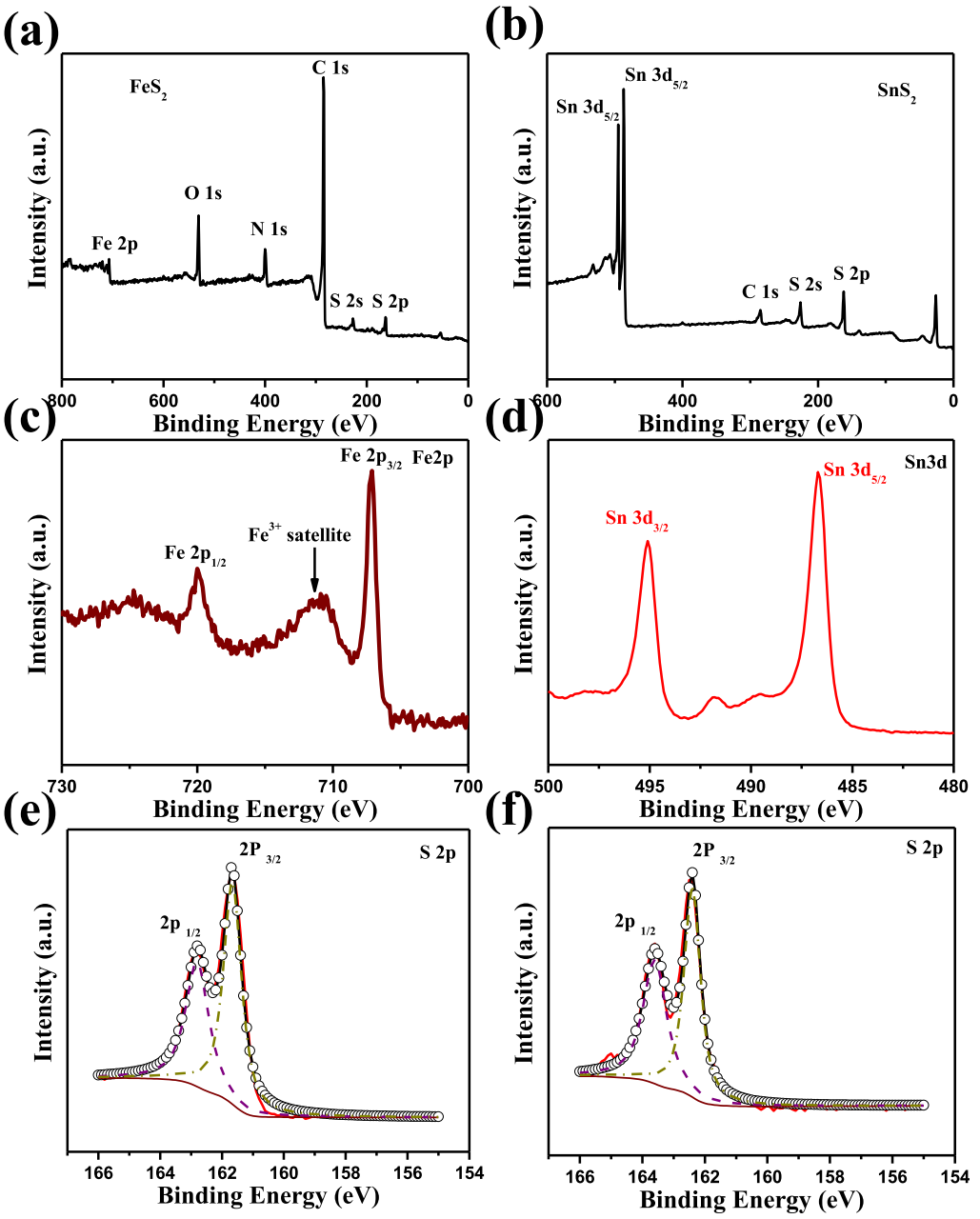

Figure 7. Spectroscopic analysis of FeS_2/C and SnS_2/C. The XPS spectra of (a) full elements, (c) Fe 2p, and (e) S 2p of FeS_2/C sample. The XPS spectra of (b) full elements, (d) Sn 3d, and (f) S 2p of SnS_2/C sample.

pulverization, resulting in poor contact with the current collector and greater resistance.

CONCLUSIONS

In this work, we used waste biomass crab shells as a carbon source to synthesize SnS_2/C and FeS_2/C composite anodes through simple hydrothermal method. Biomass carbon source has the advantages of low cost, porous fibers, and a large specific surface area, which can greatly improve the conductivity of the composite. Synthetic SnS_2/C and FeS_2/C samples not only have the high capacities of transition-metal sulfides but also own enhanced conductivity and transmission capabilities by combining with low-cost crab carbon. When used as the anode of sodium-ion batteries, the discharge specific capacity of the electrode is 416.5 and 393.8 mA h g^{-1} at the current density of 0.5 A g^{-1}. This research provides an efficient route to utilize low-cost waste raw materials to construct high-specific energy sodium-ion batteries.

ASSOCIATED CONTENT

Supporting Information

The Supporting Information is available free of charge at https://pubs.acs.org/doi/10.1021/acsomega.2c06429.

Materials characterization, measurement of the electrochemical properties, calculation formula of capacity retention, and SEM images of crab carbon (PDF)

AUTHOR INFORMATION

Corresponding Authors

Yun Chen − *Medical Engineering and Technology Research Center, School of Radiology, Shandong First Medical*

https://doi.org/10.1021/acsomega.2c06429
ACS Omega 2023, 8, 9145−9153

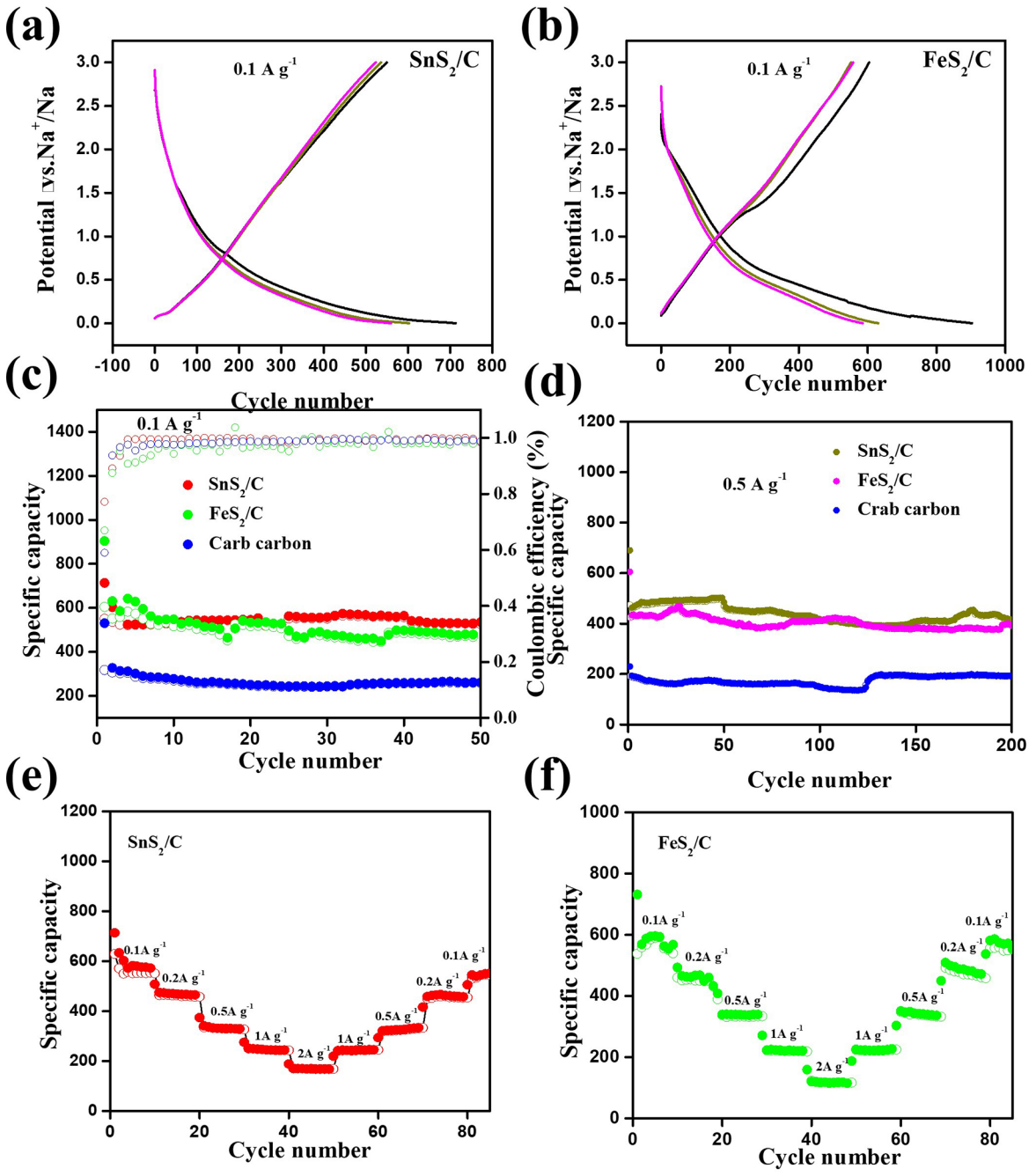

Figure 8. Typical discharge/charge curves of (a) SnS_2/C and (b) FeS_2/C composites at the current density of 0.1 A g^{-1}. The cycling performance of crab carbon, SnS_2/C, and FeS_2/C at the current densities of (c) 0.1 A g^{-1} and (d) 0.5 A g^{-1} between 0.005 and 3.0 V. Rate capability of charge capacity of (e) SnS_2/C and (f) FeS_2/C at different current densities.

University, Shandong Academy of Medical Sciences, Taian 271000, China; Email: ychen20220206@163.com

Hongbin Liu − *Graduate School of Life Science and Systems Engineering, Kyushu Institute of Technology, Kitakyushu 808-0196, Japan*; Email: hongbin0808@163.com

Tingli Ma − *Graduate School of Life Science and Systems Engineering, Kyushu Institute of Technology, Kitakyushu 808-0196, Japan; College of Materials and Chemistry, China Jiliang University, Hangzhou 310018, P. R. China*; orcid.org/0000-0001-9128-1546; Email: tinglima@life.kyutech.ac.jp

Author

Yue Zhao − *Graduate School of Life Science and Systems Engineering, Kyushu Institute of Technology, Kitakyushu 808-0196, Japan; College of Materials and Chemistry, China Jiliang University, Hangzhou 310018, P. R. China*

Complete contact information is available at: https://pubs.acs.org/10.1021/acsomega.2c06429

Notes

The authors declare no competing financial interest.

https://doi.org/10.1021/acsomega.2c06429
ACS Omega 2023, 8, 9145−9153

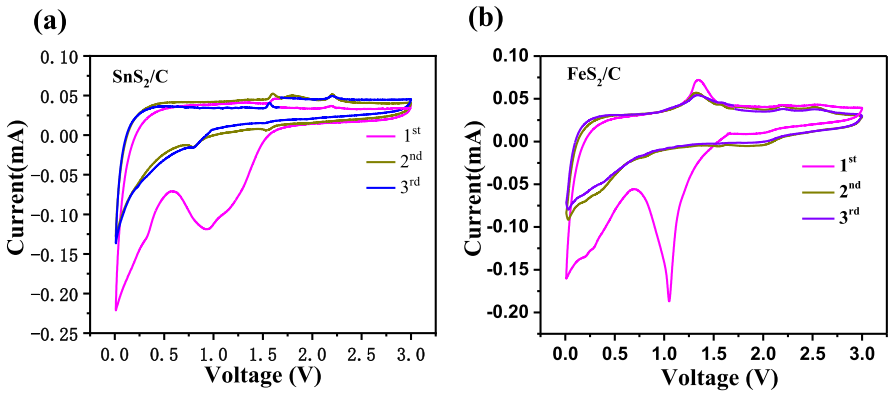

Figure 9. Cyclic voltammograms of (a) SnS_2/C and (b) FeS_2/C samples at a scan rate of 0.1 mV s^{-1} between 0.01 and 3 V.

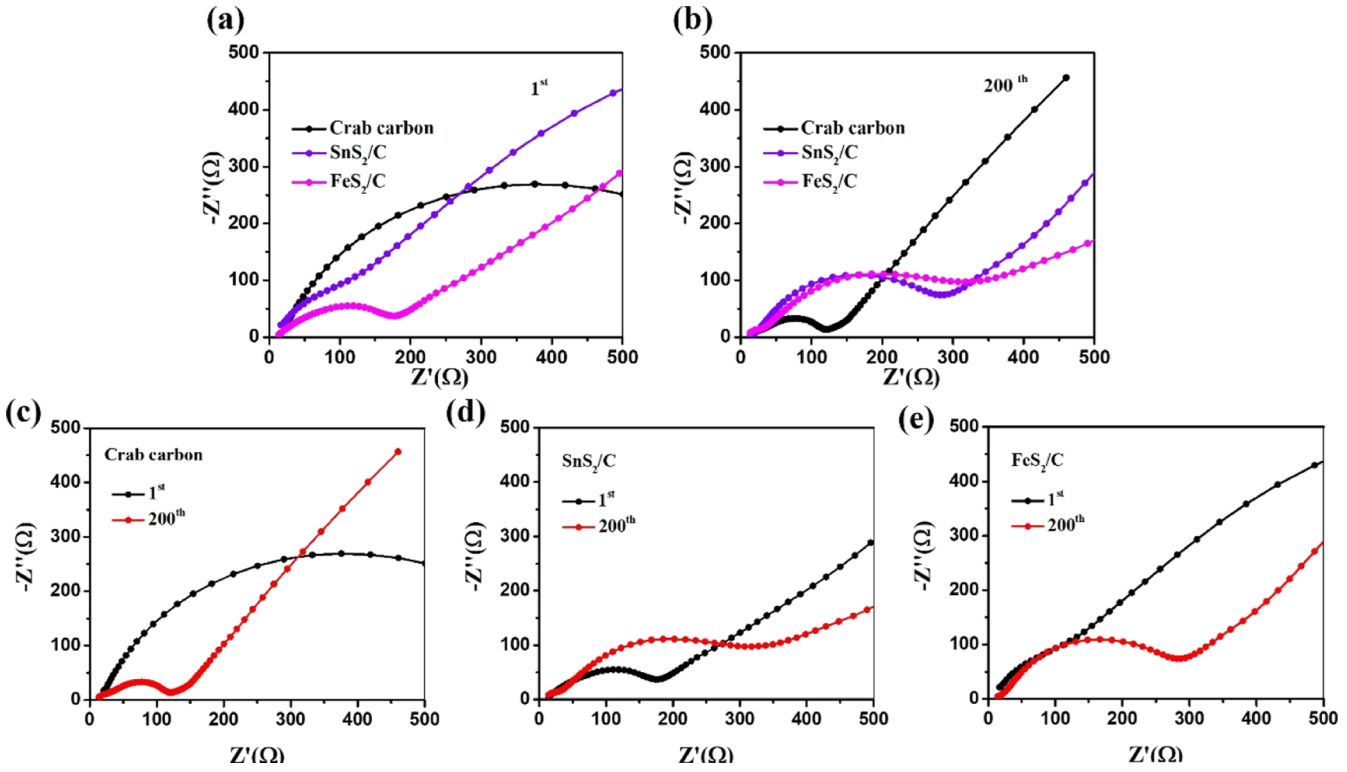

Figure 10. EIS comparison of the crab carbon, SnS_2/C, and SnS_2/C samples at the (a) 1st and (b) 200th cycles. The EIS display of (c) crab carbon, (d) SnS_2/C, and (e) SnS_2/C samples, respectively.

■ ACKNOWLEDGMENTS

This work was conducted at the Kitakyushu Foundation for the Advancement of Industry, Science and Technology, Semiconductor Center, and supported by "Nanotechnology Platform Program" of the Ministry of Education, Culture, Sports, Science and Technology (MEXT), Japan, Grant Number JPMXP09F-19-FA-0029, and KAGENHI Grant-in-Aid for Scientific Research(B), no. 19H02818, the National Natural Science Foundation of China (grant nos. 51772039 and 51972293), the Taishan Scholars Program of Shandong Province (TS201712065), and the Academic Promotion Program of Shandong First Medical University (2019QL009).

■ REFERENCES

(1) Xu, X.; Ying, H.; Zhang, S.; Meng, Z.; Yan, X.; Han, W.-Q. Biomass-Derived 3D Interconnected Porous Carbon-Encapsulated Nano-FeS2 for High-Performance Lithium-Ion Batteries. *ACS Appl. Energy Mater.* **2020**, *3*, 5589−5596.

(2) Han, L.; Zhong, Y.-l.; Su, Y.; Wang, L.-t.; Zhu, L.-s.; Fei, X.-f.; Dong, Y.-z.; Hong, G.; Zhou, Y.-t.; Fang, D. Nanocomposites based on 3D macroporous biomass carbon with SnS2 nanosheets hierarchical structure for efficient removal of hexavalent chromium. *Chem. Eng. J.* **2019**, *369*, 1138−1149.

(3) Lu, Z.; Zhai, Y.; Wang, N.; Zhang, Y.; Xue, P.; Guo, M.; Tang, B.; Huang, D.; Wang, W.; Bai, Z.; Dou, S. FeS2 nanoparticles embedded in N/S co-doped porous carbon fibers as anode for sodium-ion batteries. *Chem. Eng. J.* **2020**, *380*, 122455.

(4) Lu, X.; Liu, D.; Han, T.; Zhu, M.; Ryu, S. O.; Huang, J. A facile synthesis of sandwich-structured SnS2@reduced graphene oxide with high performance for lithium-ion battery anode. *J. Alloys Compd.* **2018**, *765*, 1061−1071.

(5) Xu, X.; Meng, Z.; Zhu, X.; Zhang, S.; Han, W.-Q. Biomass carbon composited FeS 2 as cathode materials for high-rate rechargeable lithium-ion battery. *J. Power Sources* **2018**, *380*, 12−17.

https://doi.org/10.1021/acsomega.2c06429
ACS Omega 2023, 8, 9145−9153

(6) Ou, X.; Cao, L.; Liang, X.; Zheng, F.; Zheng, H. S.; Yang, X.; Wang, J. H.; Yang, C.; Liu, M. Fabrication of SnS2/Mn2SnS4/Carbon Heterostructures for Sodium-Ion Batteries with High Initial Coulombic Efficiency and Cycling Stability. *ACS Nano* **2019**, *13*, 3666−3676.
(7) Li, D.; Sun, Y.; Chen, S.; Yao, J.; Zhang, Y.; Xia, Y.; Yang, D. Highly Porous FeS/Carbon Fibers Derived from Fe-Carrageenan Biomass: High-capacity and Durable Anodes for Sodium-Ion Batteries. *ACS Appl. Mater. Interfaces* **2018**, *10*, 17175−17182.
(8) Cao, L.; Gao, X.; Zhang, B.; Ou, X.; Zhang, J.; Luo, W. B. Bimetallic Sulfide Sb2S3@FeS2 Hollow Nanorods as High-Performance Anode Materials for Sodium-Ion Batteries. *ACS Nano* **2020**, *14*, 3610−3620.
(9) Lu, S.; Jiang, J.; Yang, H.; Zhang, Y. J.; Pei, D. N.; Chen, J. J.; Yu, Y. Phase Engineering of Iron-Cobalt Sulfides for Zn-Air and Na-Ion Batteries. *ACS Nano* **2020**, *14*, 10438−10451.
(10) Kashale, A. A.; Dwivedi, P. K.; Sathe, B. R.; Shelke, M. V.; Chang, J. Y.; Ghule, A. V. Biomass-Mediated Synthesis of Cu-Doped TiO2 Nanoparticles for Improved-Performance Lithium-Ion Batteries. *ACS Omega* **2018**, *3*, 13676−13684.
(11) Bai, M.; Tang, X.; Sun, C.; Zhang, Y.; Wu, W.; Li, S.; Liu, S.; Zhao, W.; Ma, Y. Ternary Anode Design for Sustainable Battery Technology: An Off-Stoichiometric Sn/SnSiOx+2@C Composite Recycled from Biomass. *ACS Sustainable Chem. Eng.* **2019**, *7*, 12563.
(12) Oh, P.; Lee, H.; Park, S.; Cha, H.; Kim, J.; Cho, J. Improvements to the Overpotential of All-Solid-State Lithium-Ion Batteries during the Past Ten Years. *Adv. Energy Mater.* **2020**, *10*, 2000904.
(13) Yin, X.; Sarkar, S.; Shi, S.; Huang, Q. A.; Zhao, H.; Yan, L.; Zhao, Y.; Zhang, J. Recent Progress in Advanced Organic Electrode Materials for Sodium-Ion Batteries: Synthesis, Mechanisms, Challenges and Perspectives. *Adv. Funct. Mater.* **2020**, *30*, 1908445.
(14) Fang, G.; Wu, Z.; Zhou, J.; Zhu, C.; Cao, X.; Lin, T.; Chen, Y.; Wang, C.; Pan, A.; Liang, S. Observation of Pseudocapacitive Effect and Fast Ion Diffusion in Bimetallic Sulfides as an Advanced Sodium-Ion Battery Anode. *Adv. Energy Mater.* **2018**, *8*, 1703155.
(15) Lin, X. M.; Chen, J. H.; Fan, J. J.; Ma, Y.; Radjenovic, P.; Xu, Q. C.; Huang, L.; Passerini, S.; Tian, Z. Q.; Li, J. F. Synthesis and Operando Sodiation Mechanistic Study of Nitrogen-Doped Porous Carbon Coated Bimetallic Sulfide Hollow Nanocubes as Advanced Sodium Ion Battery Anode. *Adv. Energy Mater.* **2019**, *9*, 1902312.
(16) Zhang, Y.; Wang, P.; Yin, Y.; Liu, N.; Song, N.; Fan, L.; Zhang, N.; Sun, K. Carbon coated amorphous bimetallic sulfide hollow nanocubes towards advanced sodium ion battery anode. *Carbon* **2019**, *150*, 378−387.
(17) Lv, J.; Bai, D.; Yang, L.; Guo, Y.; Yan, H.; Xu, S. Bimetallic sulfide nanoparticles confined by dual-carbon nanostructures as anodes for lithium-/sodium-ion batteries. *Chem. Commun.* **2018**, *54*, 8909−8912.
(18) Chen, Y.; Shi, X.; Lu, B.; Zhou, J. Concave Engineering of Hollow Carbon Spheres toward Advanced Anode Material for Sodium/Potassium-Ion Batteries. *Adv. Energy Mater.* **2022**, *15*, 2202851.
(19) Hou, T.; Yue, S.; Sun, X.; Fan, A.; Chen, Y.; Wang, M.; Cai, S.; Zheng, C.; Liao, B.; Zhao, J. Nitrogen-Doped graphene coated FeS2 microsphere composite as high-performance anode materials for sodium-ion batteries enhanced by the chemical and structural synergistic effect. *Appl. Surf. Sci.* **2020**, *505*, 144633.
(20) Jing, P.; Wang, Q.; Wang, B.; Gao, X.; Zhang, Y.; Wu, H. Encapsulating yolk-shell FeS2@carbon microboxes into interconnected graphene framework for ultrafast lithium/sodium storage. *Carbon* **2020**, *159*, 366−377.
(21) Shao, L.; Hong, J.; Wang, S.; Wu, F.; Yang, F.; Shi, X.; Sun, Z. Urchin-like FeS2 hierarchitectures wrapped with N-doped multi-wall carbon nanotubes@rGO as high-rate anode for sodium ion batteries. *J. Power Sources* **2021**, *491*, 229627.
(22) Xia, J.; Liu, L.; Jamil, S.; Xie, J.; Yan, H.; Yuan, Y.; Zhang, Y.; Nie, S.; Pan, J.; Wang, X.; Cao, G. Free-standing SnS/C nanofiber anodes for ultralong cycle-life lithium-ion batteries and sodium-ion batteries. *Energy Storage Mater.* **2019**, *17*, 1−11.
(23) Gao, T.; Zhang, Q.; Li, L.; Zhou, X.; Li, L.; Li, H.; Zhai, T. 2D Ternary Chalcogenides. *Adv. Opt. Mater.* **2018**, *6*, 1800058.
(24) Zuo, G.; Wang, Y.; Teo, W. L.; Xie, A.; Guo, Y.; Dai, Y.; Zhou, W.; Jana, D.; Xian, Q.; Dong, W.; Zhao, Y. Ultrathin ZnIn2 S4 Nanosheets Anchored on Ti3 C2 TX MXene for Photocatalytic H2 Evolution. *Angew. Chem.* **2020**, *59*, 11287−11292.
(25) Zhang, W.; Pan, Z.-Z.; Lv, W.; Lv, R.; Shen, W.; Kang, F.; Yang, Q.-H.; Weng, Y.; Huang, Z.-H. Wasp nest-imitated assembly of elastic rGO/p-Ti3C2Tx MXene-cellulose nanofibers for high-performance sodium-ion batteries. *Carbon* **2019**, *153*, 625−633.
(26) Haridas, A. K.; Heo, J.; Li, X.; Ahn, H.-J.; Zhao, X.; Deng, Z.; Agostini, M.; Matic, A.; Ahn, J.-H. A flexible and free-standing FeS/sulfurized polyacrylonitrile hybrid anode material for high-rate sodium-ion storage. *Chem. Eng. J.* **2020**, *385*, 123453.
(27) Zhu, H.; Jia, Z.; Chen, Y.; Weadock, N.; Wan, J.; Vaaland, O.; Han, X.; Li, T.; Hu, L. Tin Anode for Sodium-Ion Batteries Using Natural Wood Fiber as a Mechanical Buffer and Electrolyte Reservoir. *Nano Lett.* **2013**, *13*, 3093−3100.
(28) Guan, S.; Wang, T.; Fu, X.; Fan, L.-Z.; Peng, Z. Coherent SnS2/NiS2 hetero-nanosheet arrays with fast charge transfer for enhanced sodium-ion storage. *Appl. Surf. Sci.* **2020**, *508*, 145241.
(29) Li, J.; Han, L.; Li, Y.; Li, J.; Zhu, G.; Zhang, X.; Lu, T.; Pan, L. MXene-decorated SnS2/Sn3S4 hybrid as anode material for high-rate lithium-ion batteries. *Chem. Eng. J.* **2020**, *380*, 122590.
(30) Dai, J.; Liao, J.; He, M.; Yang, M.; Wu, K.; Yao, W. Si@SnS2 -Reduced Graphene Oxide Composite Anodes for High-Capacity Lithium-Ion Batteries. *ChemSusChem* **2019**, *12*, 5092−5098.
(31) Zhao, B.; Song, D.; Ding, Y.; Li, W.; Wang, Z.; Jiang, Y.; Zhang, J. Size-tunable SnS2 nanoparticles assembled on graphene as anodes for high performance lithium/sodium-ion batteries. *Electrochim. Acta* **2020**, *354*, 136730.
(32) Mao, W.; Ding, Y.; Li, M.; Ma, C.; Gong, H.; Pan, J.; Zhang, S.; Qian, Y.; Bao, K. Synthesis and electrochemical characterization of 2D SnS2/RGO as anode material in sodium-ion batteries. *J. Alloys Compd.* **2021**, *855*, 157209.
(33) Wang, L.; Zhao, Q.; Wang, Z.; Wu, Y.; Ma, X.; Zhu, Y.; Cao, C. Cobalt-doping SnS2 nanosheets towards high-performance anodes for sodium ion batteries. *Nanoscale* **2020**, *12*, 248−255.
(34) Liu, J.; Xu, Y.-G.; Kong, L.-B. High-capacity and fast Na-ion diffusion rate three-dimensional MoS2/SnS2-RGO anode for advanced sodium-ion batteries and sodium-ion capacitors. *Solid State Ionics* **2020**, *355*, 115416.
(35) Hu, Y.; Fan, L.; Rao, A. M.; Yu, W.; Zhuoma, C.; Feng, Y.; Qin, Z.; Zhou, J.; Lu, B. Cyclic-anion salt for high-voltage stable potassium-metal batteries. *Natl. Sci. Rev.* **2022**, *9*, nwac134.
(36) Liu, Z.; Zhang, S.; Qiu, Z.; Huangfu, C.; Wang, L.; Wei, T.; Fan, Z. Tin Nanodots Derived From Sn(2+) /Graphene Quantum Dot Complex as Pillars into Graphene Blocks for Ultrafast and Ultrastable Sodium-Ion Storage. *Small* **2020**, *16*, No. e2003557.
(37) Shen, Y.; Deng, S.; Liu, P.; Zhang, Y.; Li, Y.; Tong, X.; Shen, H.; Liu, Q.; Pan, G.; Zhang, L.; Wang, X.; Xia, X.; Tu, J. Anchoring SnS2 on TiC/C Backbone to Promote Sodium Ion Storage by Phosphate Ion Doping. *Small* **2020**, *16*, No. e2004072.
(38) Zhang, J.; Liu, Y.; Liu, H.; Song, Y.; Sun, S.; Li, Q.; Xing, X.; Chen, J. Urchin-Like Fe3 Se4 Hierarchitectures: A Novel Pseudocapacitive Sodium-Ion Storage Anode with Prominent Rate and Cycling Properties. *Small* **2020**, *16*, 2000504.
(39) Shen, F.; Fu, J.; Zhang, X.; Qi, X. Crab Shell-Derived Lotus Rootlike Porous Carbon for High Efficiency Isomerization of Glucose to Fructose under Mild Conditions. *ACS Sustainable Chem. Eng.* **2019**, *7*, 4466−4472.
(40) Fu, M.; Chen, W.; Zhu, X.; Yang, B.; Liu, Q. Crab shell derived multi-hierarchical carbon materials as a typical recycling of waste for high performance supercapacitors. *Carbon* **2019**, *141*, 748−757.
(41) Liu, H.-J.; Wang, X.-M.; Cui, W.-J.; Dou, Y.-Q.; Zhao, D.-Y.; Xia, Y.-Y. Highly ordered mesoporous carbon nanofiber arrays from a

https://doi.org/10.1021/acsomega.2c06429
ACS Omega 2023, 8, 9145−9153

crab shell biological template and its application in supercapacitors and fuel cells. *J. Mater. Chem.* **2010**, *20*, 4223.
(42) Kim, H. S.; Kang, M. S.; Lee, S.; Lee, Y.-W.; Yoo, W. C. N-doping and ultramicroporosity-controlled crab shell derived carbons for enhanced CO2 and CH4 sorption. *Microporous Mesoporous Mater.* **2018**, *272*, 92−100.
(43) Shi, W.; Chang, B.; Yin, H.; Zhang, S.; Yang, B.; Dong, X. Crab shell-derived honeycomb-like graphitized hierarchically porous carbons for satisfactory rate performance of all-solid-state supercapacitors. *Sustainable Energy Fuels* **2019**, *3*, 1201−1214.
(44) Huang, J.; Zhang, J.; Han, F.; Cai, J.; Chen, Y.; Liu, H. An in situ solid-electrolyte interphase strategy to inhibit polysulfide shuttles of FeS2-based cathode material. *Chem. Eng. J.* **2022**, *427*, 131765.
(45) Chen, C.; Liang, Q.; Wang, G.; Liu, D.; Xiong, X. Grain-boundary-rich artificial SEI layer for high-rate lithium metal anodes. *Adv. Funct. Mater.* **2022**, *32*, 2107249.

https://doi.org/10.1021/acsomega.2c06429
ACS Omega 2023, 8, 9145−9153